Volume Scattering Analysis of Titan's Lakes and Seas via Cassini RADAR Altimetric Observations

L. Gambacorta, M. Mastrogiuseppe, M C Raguso, V. Poggiali, Daniel Cordier, K K Farnsworth, R. Seu

Volume Scattering Analysis of Titan's lakes and seas via Cassini RADAR Altimetric Observations

L. Gambacorta, M. Mastrogiuseppe, M. C. Raguso, V. Poggiali, D. Cordier, K. K. Farnsworth, and R. Seu

***Abstract*— This paper presents a study to assess the characteristics of particles or bubbles possibly present on Titan's lakes and seas using Cassini RADAR observations when operating in altimetry/sounder mode. We developed an analytical model for the Surface-to-Volume power Ratio (SVR) which includes the principles of radiative equilibrium and Mie scattering theory. The model considers the effects due to extinction phenomena and can be used to extract valuable information on the presence of dust particles or bubbles in Titan's liquid bodies. The absence of volume scattering in the altimetric waveforms is used to constrain the maximum density at various radii of the possible presence of nitrogen bubbles or solid particles, such as water ice, nitriles, and tholins.**

***Index Terms*— Cassini, Titan, radar altimetry, radar sounder, Mie scattering theory, radiative equilibrium.**

NOMENCLATURE

c	Speed of light (approx. 3e8 m/s)
α	Blackman window parameter
P_a, P_{sc}	Absorbed and scattering power, W
Q_a, Q_{sc}, Q_e	Absorption, scattering and extinction cross-section
S_i, S_{sc}	Incident and scattered power density, W/m^2
ξ_a, ξ_{sc}, ξ_e	Absorption, scattering and extinction efficiencies
σ_b	Backscattering radar cross-section, m^2
Ω	Solid angle, sr
θ	Elevation radiation angle, rad
ϕ	Azimuth radiation angle, rad
n	Refraction index ratio
λ	Radar wavelength, m
r	Particle radius, m
$\varepsilon_i, \varepsilon_h, \varepsilon_m$	Inclusion, host material and mixture complex dielectric constants
tgδ	Material loss tangent
P_i	Incident power, W
P_S, P_{SS}	Surface and subsurface reflected power, W
Γ_s or R_{12}^2	Fresnel reflectivity
σ_s	Surface radar cross-section, m^2
R	Radar altitude, m
σ_h	Surface root-mean square height, m
k	Wave number, 1/m
P_t	Transmitted power, W
P_S	Surface power, W
P_V	Volume Power, W
P_N	Noise power, W
$P_{N,int}$	Integrated Noise power, W
G	Antenna gain
$\vartheta_{3\,dB}$	Antenna beamwidth at -3 dB, rad
τ	Two-way attenuation
σ	Radar cross-section, m^2
σ_0^V	Backscattering volume coefficient, 1/m
k_a, k_s, k_e	Absorption, scattering and extinction volume coefficients, 1/m
r	Particle radius, m
v_i	Volume inclusion fraction
N_V, N	Particles density, n/m^3
n(r)	Particles density probability density function
P_V	Volume power, W
S_V	Volume power density, W/m
P_N	Integrated noise power, W
SVR	Surface-to-Volume power Ratio
SNR	Signal-to-Noise Ratio (P_s/P_N)
SNR_{int}	Integrated Signal-to-Noise Ratio

I. INTRODUCTION

The Cassini spacecraft's RADAR Mapper played a crucial role in unveiling the surface of Saturn's largest moon, Titan, by providing unparalleled details of its surface throughout the mission [1], [2]. The instrument was specifically designed to operate in various modes, such as Synthetic Aperture Radar (SAR), Altimeter, Scatterometer and Radiometer [3]. In 48 flybys, Cassini covered 46% of Titan's surface capturing SAR images with a resolution better than 1 km and acquiring 40 topographic profiles in altimetry mode [4]. With its RADAR instrument, Cassini observed topographic and geological features such as dunes, mountains, canyon and the presence of vast lakes and seas at the moon's poles [5], [6], [7], [8], [9], [10]. The composition of these reservoirs are liquid hydrocarbons, primarily

L. Gambacorta, M. Mastrogiuseppe and R. Seu are with the Dipartimento di Ingegneria dell'Informazione, Elettronica e Telecomunicazioni (DIET), La Sapienza Università di Roma, Roma, RM, Italia (e-mails: letizia.gambacorta@uniroma1.it, marco.mastrogiuseppe@uniroma1.it, roberto.seu@uniroma1.it). M.C. Raguso was with the Dipartimento di Ingegneria dell'Informazione, Elettronica e Telecomunicazioni (DIET), Sapienza Università di Roma, Roma, RM, Italy, now is with Jet Propulsion Laboratory, California Institute of Technology, Pasadena, CA, 91109 USA (e-mail: maria.raguso@jpl.nasa.gov). This work was done as a private venture and not in the author's capacity as an employee of the Jet Propulsion Laboratory, California Institute of Technology. D. Cordier is with the French Center for Scientific Research (CNRS), Paris, France (e-mail: daniel.cordier@cnrs.fr). K. K. Farnsworth is with NASA Goddard Space Flight Center (GSFC), Greenbelt, Maryland (e-mail: kendra.farnsworth@nasa.gov).

methane and ethane, with a percentage of dissolved atmospheric nitrogen [11], [12]. In May 2013, nadir-pointed altimetry data acquired over Ligeia Mare, revealed two distinct echoes, one from the surface and the other from its seabed. This measurement demonstrated that the instrument was able to operate as a sounder, capable of probing Titan's seas and lakes down to hundreds of meters and providing valuable insights of the liquid composition [12]. This detection has then been followed by the bathymetry of other

Titan seas and lakes, including Ontario Lacus, Punga Mare, Kraken Mare and Winnipeg Lacus [13], [14], [15], [16], [17]. In 2016, a comparison between multiple SAR observations led to the detection of over-bright transient backscattering features at the surface of Ligeia Mare [18]. These features, named the "*Magic Islands"*, have not been attributed to artifacts (azimuth and range aliasing and scalloping) or observation geometry changes and are likely explained as the result of ephemeral phenomena associated with floating and/or suspended solids, rising gas bubbles or waves from topographically funneled wind [19], [20].

The presence of solid particles in Titan's lakes and seas has been hypothesized as the result of complex aeolian atmospheric processes, as well as fluvial transport of sediments from the crust or rain washing [21], [22], [23]. Aerosol and water ice haze particles originate in the upper atmosphere and can coalesce and settle on the surface, forming larger sand-sized particles [24], [25]. Such phenomena would also explain the formation of dunes at Titan's equator and the presence of evaporites at the bottom of dry lake beds and edges of evaporating lakes [26], [27], [28].

Among solid particles, water ice inclusions represent a possible explanation for the "*Magic Island"* formation because of their insolubility in liquid hydrocarbons and as the main constituent of Titan's crust [29]. Furthermore, Titan's complex atmospheric photochemical chemistry provides organic material to settle onto its surface. These organics include acetylene, hydrogen cyanide and nitriles [29]. Such molecules dissolve in the hydrocarbon mixture and precipitate out of solution when the solubility is exceeded. [30], [31]. As the density of most of these particles is higher than the host liquid's, their presence is assumed to be the result of an ascending stream, uplifting the particles, and preventing them from sinking [32], [33].

The occurrence of nitrogen bubbles in Titan's seas and lakes has been widely investigated and associated with liquid supersaturation of nitrogen gas [34]. Experimental studies suggest that nitrogen exsolution from mixed ethane/methane solutions could be triggered by events that would decrease the solubility of dissolved nitrogen gas, including an increase in temperature, and an increase in ethane concentration (i.e., due to rain drops or rainfall runoff), possibly leading to the overturning of stratified lakes [35], [36], [37], [38]. Other theoretical studies investigate bubble nucleation and growth and developed a radiative transfer model appropriate for describing bubble reflectivity at Titan lake conditions [39], [40]. They identify the seabed as the most plausible location for the generation of bubbles, leading to a radar reflectivity comparable to the one observed during the "*Magic Island"*.

The objective of our research is to assess the presence of particles or bubbles in Titan's lakes and seas and determine their size and density by means of a volume scattering analysis of

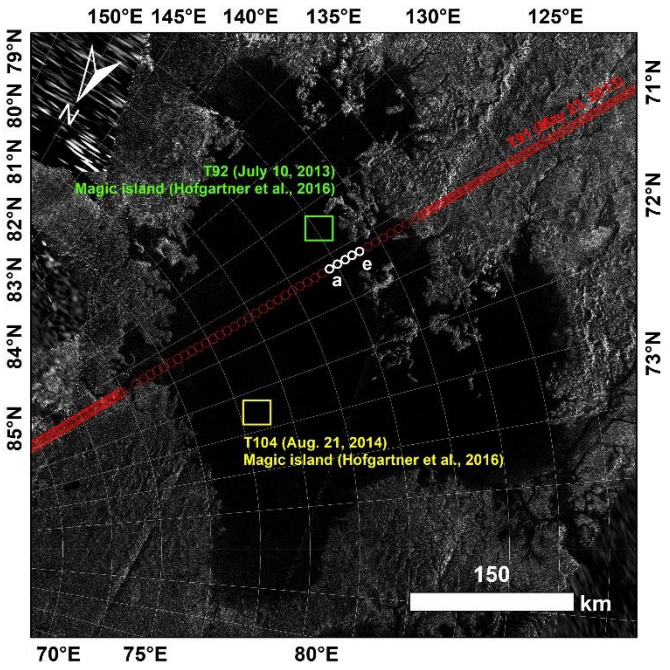

Fig 1. Cassini ground-track over Titan's Ligeia Mare during T91 flyby is presented in red, where each circle represent an altimetric acquisition/burst. Bursts highlighted in white (a-e) are the ones under investigation in this manuscript (see Fig. 2). The green and yellow squares refer to the location at which the Magic Island has been observed during flybys T92 and T104.

Cassini altimetric data. Based on the Mie scattering assumptions and the classical radiative transfer theory, we derive a comprehensive expression for the volume scattering return, specifically for the case of a beam-limited acquisition geometry and a flat surface. By modelling the backscattered surface and volume powers, we derive an expression of the Surface-to-Volume scattering power Ratio (SVR) as a function of particles radius and volume inclusion fraction for different host-inclusion mixture scenarios. We constrain the maximum size of gaseous/solid inclusions at various densities in the probed sea by comparing the model with the measured SVR. Our results highlight the impact of inclusions properties on the radar echo in the case of a liquid host medium.

This manuscript is structured as follows. Section II describes Cassini altimetry dataset and processing. Section III presents a brief review of the Mie Theory, which serves as a foundation for our study. Section IV is dedicated to the analytical derivation of the SVR and the description of its behavior. Finally, in Section V, we apply the volume scattering analysis to the Cassini altimetric observations at Ligeia mare and present our results.

II. Dataset and Processing

We used altimetric data acquired by the Cassini RADAR, operating at Ku-band (f_c=13.78 GHz, $\lambda = 2.17$ cm) and available on the NASA Planetary Data Science (PDS) node website (https://pds-imaging.jpl.nasa.gov/volumes/radar.html) in the format of Long-Burst Data Record (LBDR) [41].

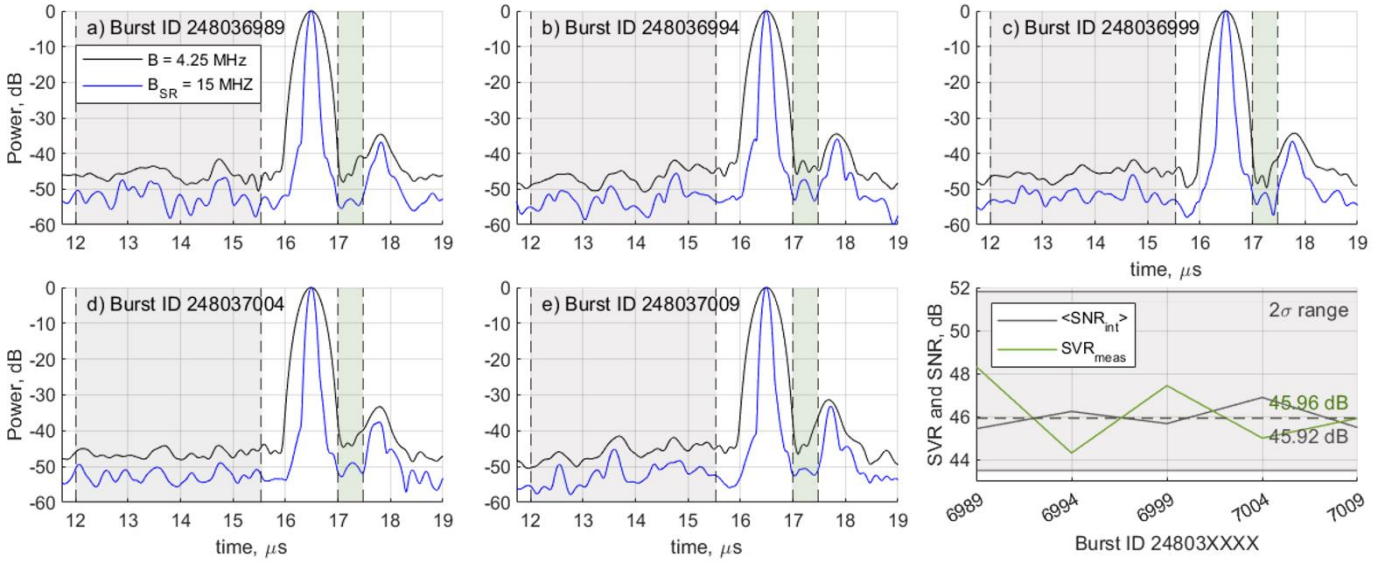

Fig. 2. a) - e) The five selected altimetric waveforms acquired by the Cassini RADAR during T91 flyby over Ligeia Mare before and after Super-Resolution in black and blue, respectively. We integrate the sounding waveform in the area highlighted in green from 17.0 to 17.5 μs. Noise is integrated before the surface echo by averaging the contributions obtained in a sliding window with the same size and moving from 12.0 to 15.5 μs, highlighted in grey. f) Results from pulse-by-pulse signal and noise integration (green and gray solid lines) and their average values (horizontal dashed lines). We measure an integrated signal power of 45.96 dB and an integrated noise power of 42.96 dB, thus we can assume that there is no remarkable contribution of volume scattering effects.

During its operations, the Cassini RADAR operated in burst mode, transmitting frequency modulated pulses (*chirp*) with duration time of 150 μs and 4.25 MHz bandwidth.

Altimetric raw data is processed by means of the CPAD (Cassini Processing of Altimetric Data), which provides for range-compression and incoherent averaging of the pulses within a single burst [42]. With the objective of further improving the 35 m nominal range-resolution, we integrated into the CPAD an intermediate processing based on Super-Resolution (SR) techniques via the Burg method [43], [12]. This processing provides for the elimination of the 5% of samples for each side of the spectrum and exploits $M = 3$ as model order. SR techniques have been proved to be suitable for altimetric/sounder data [44], [45], [46] and widely used in planetary radar data processing [47], [48]. Previous studies have demonstrated that super-resolution techniques provide reliable results at high SNR values, such as in the current case, where the selected bursts exhibit a SNR of around 46 dB [44]. Here, we employ range-compressed signal extrapolation to enhance the Cassini RADAR bandwidth by a factor 3 (leading to a free-space vertical resolution of 11.6 m) followed by a custom weighting function able to reduce side-lobes down to 60 dB (i.e., Blackman with parameter $\alpha = 0.16$). Figure 1a–e presents the five selected pulses from the T91 flyby over Ligeia Mare, where the shallow reflector assumes almost a constant depth. We can note that after SR processing the surface and subsurface peaks are narrowed allowing a better estimation of the volume clutter contribution.

III. Mie Scattering Theory

Volume scattering occurs when an electromagnetic wave interacts with small-scale heterogeneities or irregularities in a medium, causing the wave to propagate in different directions. In the case of highly disordered systems, the electromagnetic fields scattered by the different centers are statistically independent. Therefore, the total scattered field can be regarded as an intensity-based summation of all individual contributions, which we describe through the Mie theory.

III.A. Theoretical formulation

When an electromagnetic wave interacts with a suspended particle in a host material, a fraction of the incident power is absorbed by the particle P_a, and another fraction is scattered in all directions P_{sc}. The scattering and absorbing cross-sections can be defined as the ratio of the scattered or absorbed power to the incident power density S_i respectively

$$Q_{sc} = P_{sc}/S_i \qquad Q_a = P_a/S_i \tag{1}$$

The scattering and absorption efficiencies represent the fraction of the incident power density that is scattered or absorbed by the particle of radius r respectively, normalized by the geometric cross-section

$$\xi_s = Q_{sc}/\pi r^2 \qquad \xi_a = Q_a/\pi r^2 \tag{2}$$

The total amount of power removed from the incident wave when interacting with the particle can be expressed by a summation of both these contributions, and defined respectively as extinction (or attenuation) cross-section and efficiency

$$Q_e = Q_a + Q_{sc} \qquad \xi_e = \xi_a + \xi_s \tag{3}$$

The total scattered power in all directions, $P_{sc} = \iint_{4\pi} S_{sc}(\theta,\phi) R^2 d\Omega$, where Ω represents the solid angle, can be exploited to define the backscattering radar cross-section σ_b of a single particle of suspended material. Since S_{sc} is the power density of the radiation scattered in all directions (θ, ϕ), the portion coming back towards the source is obtained by $\theta = \pi$

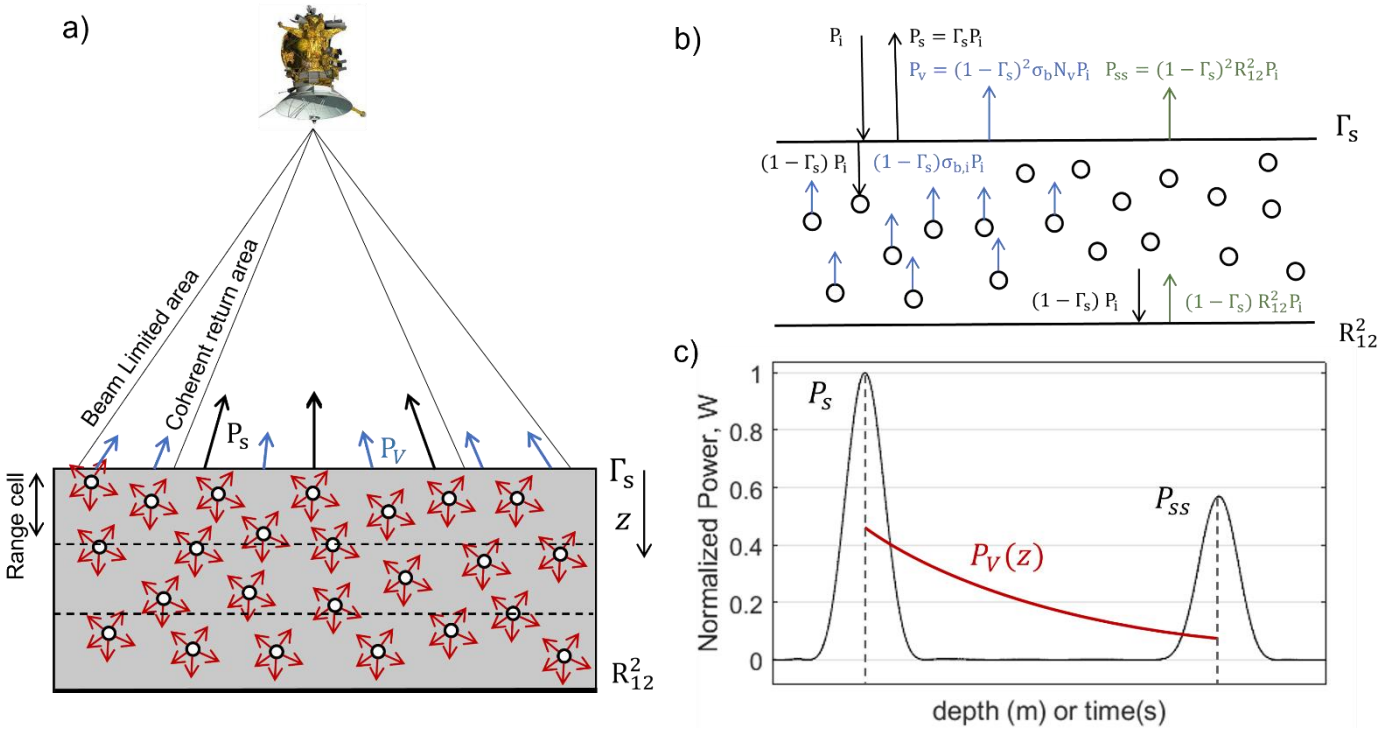

Fig. 3. a) Nadir-looking acquisition geometry of the Cassini RADAR altimeter in the case of inclusions in the probed liquid bodies. The surface power P_s refers to the coherent contribution from the Fresnel area [52], while the volume power P_v from the whole antenna footprint. b) Radiative equilibrium in a two-layers medium filled with *i* spherical inclusions. Each particle provides its contribution through its backscattering coefficient $\sigma_{b,i}$. c) Example of a sounding observation, where the normalized power backscattered from the surface and the subsurface is represented by the two sinc functions in black (P_s and P_{ss}), while the volume power $P_V(z)$ in red is characterized by an exponential decreasing trend along depth.

$$S_{sc} = \frac{S_i\,\sigma_b}{4\pi r^2} \quad \rightarrow \quad \sigma_b = 4\pi r^2\,S_{sc}\,(\pi)/S_i \qquad (4)$$

The results of Mie's solution [49] led to the following expressions for the extinction and backscattering efficiency factors in terms of converging series

$$\xi_e\,(n,\chi) = \frac{2}{\chi^2}\sum_{l=1}^{\infty}(2l+1)\,Re\{a_l + b_l\} \qquad (5)$$

$$\xi_b\,(n,\chi) = \frac{\sigma_b}{\pi r^2} = \frac{1}{\chi^2}\left|\sum_{l=1}^{\infty}(-1)^l\,(2l+1)\,(a_l + b_l)\right|^2 \qquad (6)$$

where we can define $\chi = \mathrm{k_b r} = \frac{2\pi}{\lambda_b}\mathrm{r} = \frac{2\pi \mathrm{r}}{\lambda_0}\sqrt{\varepsilon_b'}$, with $\mathrm{k_b}$ being the wave number in the background medium, λ_b and λ_0 the wavelength in the medium and in the free space respectively and ε_b' the real part of its relative dielectric constant; and with $\mathrm{n} = \mathrm{n_i}/\mathrm{n_h} = \sqrt{\varepsilon_i}/\sqrt{\varepsilon_h}$ the ratio of the complex indices of refraction of the particle inclusion and the host medium. Instead, a_l and b_l are known as the Mie coefficients.

As the material dielectric properties and particle dimensions in focus do not satisfy the necessary condition for the validity of the Rayleigh approximation ($|n\chi| \ll 1$), this study considers the general Mie Theory.

IV. Surface-to-Volume Scattering Power Ratio

This section outlines the theoretical formulation of the Surface-to-Volume scattering power Ratio (SVR). We begin by computing the surface response P_s assuming a coherent scattering regime. Subsequently, we model the volume scattering power P_V by solving the integral radar equation (10) for the case of volume backscattering [50]. Here, we incorporate the general Mie theory to account for the scattering properties of the inclusions. We then derive the SVR and describe its behavior at varying particle size and density.

A. Radiative Equilibrium and Assumptions

Nadir-looking radar observations in altimetry mode offer valuable insights into the characterization of inclusions or suspended heterogeneity in a homogeneous media. The waveform, as shown in Fig. 3c, enables the power measurements of the reflections from the surface/subsurface and the scattering from the volume, which can be utilized to constrain the size and density of inclusions.

The acquisition geometry is illustrated in Fig. 3a, where we assume a liquid column filled with spherical particles. We evaluate the volume backscattered power from the radiative equilibrium within the host medium with the reflected and transmitted powers by the surface defined as a function of the surface Fresnel coefficient $\Gamma_s = (1-\sqrt{\varepsilon_m})/(1+\sqrt{\varepsilon_m})$, function of the dielectric constant ε_m and the two-way transmittivity term $(1-\Gamma_s)^2$ respectively (see Fig. 3b). Therefore, the overall backscattering cross-section of the volume incorporates the transmittivity term as well as the backscattering individual contribution of each particle, $\sigma_{b,i}$. Furthermore, we consider the impact of signal attenuation/extinction resulting from both particle scattering and absorption phenomena, mainly influenced by

particle size and loss tangent respectively. Although not illustrated in Fig. 3b for clarity, attenuation effects are included in the derivation of the SVR, as detailed in eq. (2) and (19).

Our formulation provides for the assumption of uniformly distributed spherical inclusions with the same dielectric properties and does not account for polarization effects and multiple scattering phenomena, as suggested by previous works [19]. Moreover, we do not consider shadowing effects by particle obstruction, which do not occur when the particle radius is lower that the wavelength [51]. In our case we assume a maximum bubble radius of 2.3 cm (break-up radius), as calculated by [39], comparable to RADAR wavelength.

B. Surface backscattered power

For the surface power derivation, we assume a flat surface and a beam-limited acquisition geometry. Such hypothesis guarantees a regime of coherent backscattered power, whose contribution arises from the Fresnel area [52]. This leads to the following equation for the radar cross-section valid for the case of a spherical wavefront [53], [54]

$$\sigma_s = \pi R^2 \Gamma_s \, e^{-4\mathrm{k}\sigma_h{}^2} \tag{7}$$

where σ_h is the root mean square (rms) height of the surface, representing its vertical-scale roughness and R is the distance of the radar from the surface. In this work, we assume $\sigma_h = 0$ as Titan's lakes and seas exhibit a relatively calm surface with small-scale roughness on the order of millimeters [54], [55], [56]. Therefore P_s can be described by the following expression

$$P_s = \frac{P_t G^2 \lambda^2 \sigma_s}{(4\pi)^3 R^4} = \frac{P_t G^2 \lambda^2 \Gamma_s \pi}{(4\pi)^3 R^2} \tag{8}$$

where P_t and G are the transmitted power and the antenna gain. We compute the surface Fresnel coefficient by means of the Maxwell-Garnett mixing rule as found to be in good agreement with experimental measurements in case of uniformly distributed spherical particles up to the 10% of inclusion fraction [50]

$$\varepsilon_m = \varepsilon_h + 3v_i \, \varepsilon_h \frac{\varepsilon_i - \varepsilon_h}{\varepsilon_i + 2\varepsilon_h - v_i(\varepsilon_i - \varepsilon_h)} \tag{9}$$

where ε_m, ε_i and ε_h are the complex dielectric constant of the mixture, the inclusion and the host material respectively and v_i is the volume inclusion fraction ($0 < v_i < 1$).

C. Volume scattering power and SVR derivation

The volume power contribution can be described as an integral summation of contributions of cylinders with volume dV and with growing depth z, as illustrated in Fig. 3a.

$$P_V = \int_{A_0} \frac{P_t G^2 \lambda^2 (1-\Gamma_s)^2 e^{-2\tau}}{(4\pi)^3 R^4} d\sigma \tag{10}$$

where A_0 is the antenna footprint. The radar cross-section σ and the two-way wave attenuation τ can be expressed as

$$d\sigma = \sigma_0^V dV \quad \text{with } dV = \pi \left(\frac{\vartheta_{3\,dB}\,(R+z)}{2}\right)^2 dz \tag{11}$$

$$\tau = \int_0^z k_e(z')dz' = k_e z \tag{12}$$

where the integration volume dV in (11) refers to a beam limited configuration, considering an antenna beamwidth at –3 dB equal to $\vartheta_{3\,dB}$. In these expressions, σ_0^V and k_e represent respectively the backscattering and extinction volumetric coefficients, which account for the contribution of each scattering center through the overall number of particles per unit volume N_V

$$\sigma_0^V = \sum_{i=1}^{N_V} \sigma_{b,i}(r_i) \qquad k_e = k_s + k_a = \sum_{i=1}^{N_V} Q_e(r_i) \tag{13}$$

Under the assumption of independent scattering and neglecting multipath effects, the backscattering and the extinction caused by a collection of homogeneous and identical particles can be described by multiplying the number of inclusions by the specific scattering coefficient for a single particle

$$\sigma_0^V = N_V \, \sigma_b \qquad k_e = N_V \, Q_e \tag{14}$$

It is possible to incorporate the impact of particles of varying sizes by describing such coefficients using a continuous distribution function $n(r)$ based on the radius

$$\sigma_0^V = \int_{r_{min}}^{r_{max}} n(r) \, \sigma_b(r) dr \quad k_e = \int_{r_{min}}^{r_{max}} n(r) \, Q_e(r) dr \tag{15}$$

If we assume a Gaussian distribution function, $n(r) = \frac{N}{s\sqrt{2\pi}} \, exp\left(-\frac{(r-\bar{r})^2}{2s^2}\right)$ where $\bar{r}$ and s^2 are the mean and the variance of the variable r. We calculate the integrals within the radii values at 2-sigma, supposing that the 95% of the values is within $r_{min} = \bar{r} - 2\sqrt{s^2}$ and $r_{max} = \bar{r} + 2\sqrt{s^2}$. The number N represents particles of all sizes in unit volume and is given by

$$N = \int_{r_{min}}^{r_{max}} n(r) dr \tag{16}$$

and coincides with N_V in the case of particles with the same radius.

By substituting (11) and (12) in (10), we express P_V as an integral along the z-axis

$$P_V = \frac{P_t G^2 \lambda^2 (1-\Gamma_s)^2 \sigma_0^V}{(4\pi)^3} \frac{\pi \, \vartheta_{3\,dB}^2}{4} \int_{z_1}^{z_2} \frac{e^{-2k_e z}}{(R+z)^2} dz \tag{17}$$

This formula indicates that P_V can be described as summation of the contribution due to the particles located in the medium between depths z_1 and z_2. The magnitude of this contribution depends on their size and is weighted according to the assumed probability density function. By assuming $k_e \neq 0$ and neglecting the dependence of the radar range respect with the depth z, we solve the integral

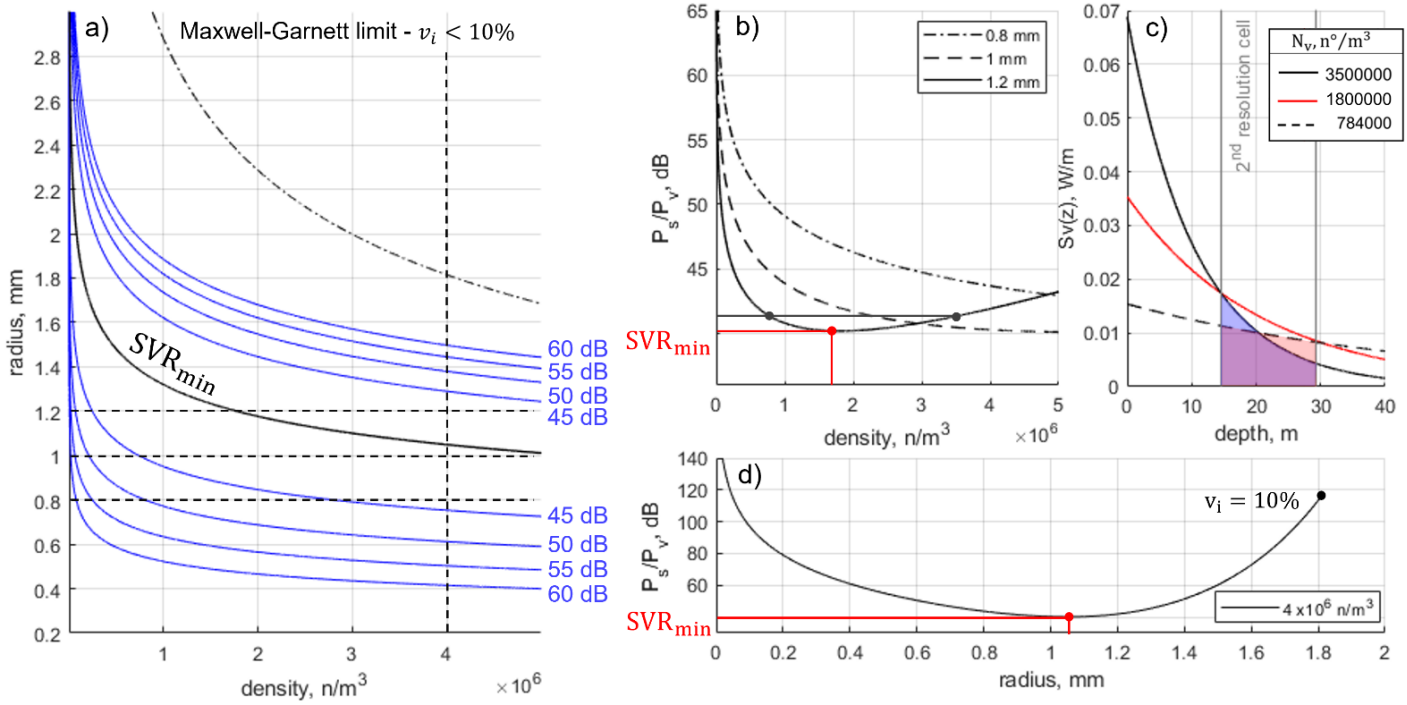

Fig. 4. a) SVR as a function of particle radius and density for the case of the SR Cassini RADAR altimetric data. The plot has been obtained considering a methane-vacuum host-inclusion scenario with particles of uniform size and by integration of $S_V(z)$ within the nominal 2nd resolution cell after super-resolution. The blue contoured lines are the SVR curves, each line refers to a different SVR value shown at the right side of the plot from 45 to 60 dB. The dashed curve refers to the Maxwell-Garnett model constraint that allows a maximum volume inclusion fraction of 10%. The black solid curve represents the minimum SVR. The horizontals and vertical dashed lines signify respectively the particle radii and density used to derive Fig. 4b and 4d. b) SVR as a function of particle density at three particle sizes (r = 0.8, 1 and 1.2 mm). c) Comparison of the volume power density along depth at r = 1.2 mm for three densities $N_V = 0.783 \times 10^6$ and 3.5×10^6 n/m^3, generating the same SVR, and 1.8×10^6 at SVR_{min}. At higher N_V the effect of the backscattering causes the volume power density to be concentrated at lower depth and to attenuate at greater depth from the surface. There exists a N_V at which the integration of the volume contribution in the selected resolution cell is maximum (red solid line). d) SVR as a function of the particle size for a fixed density value of $N_V = 4 \times 10^6\, n/m^3$.

$$P_V = \frac{P_t G^2 \lambda^2 (1-\Gamma_S)^2 \sigma_0^V}{(4\pi)^3} \frac{\vartheta_{3\,dB}^2}{8 k_e R^2} \left[e^{-2k_e z_1} - e^{-2k_e z_2} \right] \quad (18)$$

Finally, we obtain the expression for the SVR as

$$SVR = \frac{P_S}{P_V} = \frac{\Gamma_S}{(1-\Gamma_S)^2 \sigma_0^V \frac{\vartheta_{3\,dB}^2}{8 k_e} \left[e^{-2k_e z_1} - e^{-2k_e z_2} \right]} \quad (19)$$

The SVR curve is numerically computed as function of the particle radii and densities and shown in Fig. 4a for the Cassini RADAR case, considering a uniform distribution of vacuum particle size immersed into a methane host. For explanation purposes, the curve is obtained by integrating the model within the nominal super-resolution cell after Blackman windowing and varying in size according to the volume percentage of inclusions the mixture (refer to eq.(9)). Notably, it exhibits a dependence on particles radius and density N_v, which can be equally expressed in terms of volume inclusion fraction v_i (see Fig. 4b and 4d). The curve is limited according to the employed mixture model.

D. Volume Power behavior vs depth

The volume power density along the depth profile can be expressed as the integrand of equation (18)

$$S_V(z) = dP_V(z)/dz \propto (1-\Gamma_s)^2 \sigma_0^V \, e^{-2k_e z} \quad (20)$$

It carries the information at depth $z^*$of the investigated volume, which provides the specific $P_V(z^*)$ when integrated within the resolution cell. In this formula, $(1-\Gamma_s)^2 \sigma_0^V$ refers to the value at surface origin, while $e^{-2k_e z}$ to the attenuation during propagation in the medium. Scenarios with higher particle size and density result in higher σ_0^V and k_e, generating a stronger volume response at the surface and a more rapid extinction with depth, as shown in Fig. 4c. Therefore, the main contribution of P_V is concentrated at shallow depths and superimposed to the surface response. We apply SR techniques allowing to take advantage of a closest integration to the surface response.

Furthermore, the integration could lead to ambiguity in the SVR for different values of radii and/or densities. As an example, we examine in Fig. 4b and 3c the case of particles with radius of 1.2 mm and compare the $S_V(z)$ at three different densities: one at SVR minimum (red) and two resulting at a higher SVR (black). Figure 3c shows that the integrated P_V increases with higher density until reaching its maximum at SVR_{min}, after which it decreases again. We attribute this behavior to the interplay between backscattering and extinction phenomena, that for high radii and/or densities makes the $S_V(z)$ contribution to concentrate at lower depth and leading to signal extinction for higher depth. The same considerations can also be extended at different particle radii (see Fig. 4d). We solve such ambiguity

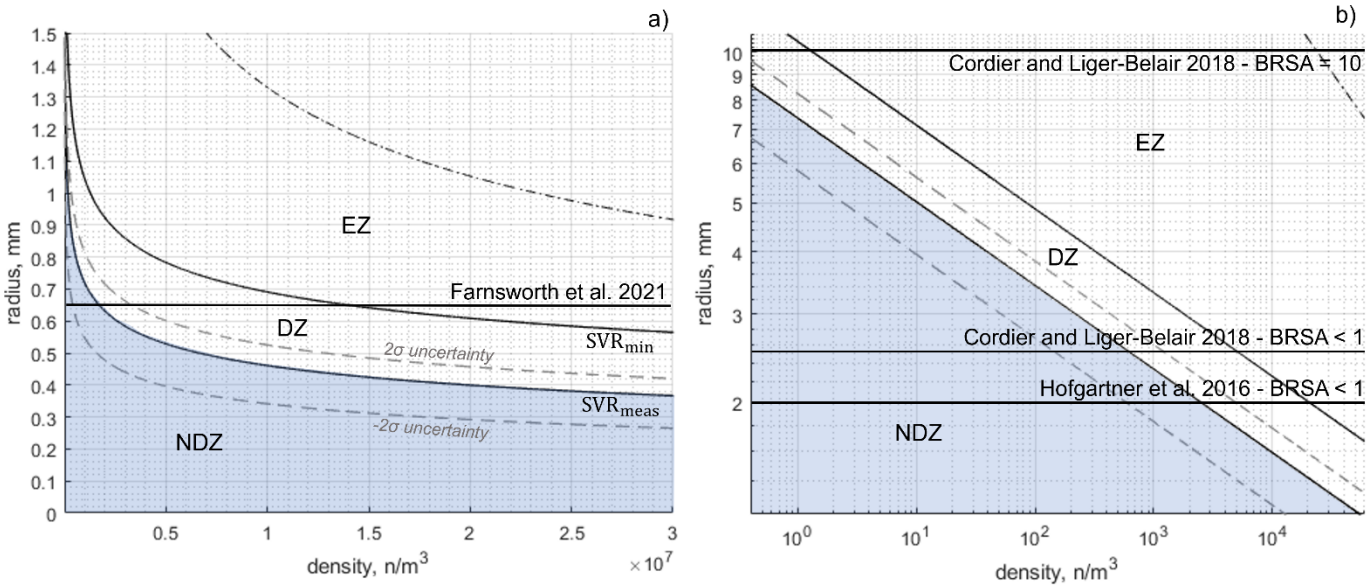

Fig. 5. SVR obtained for the case of the T91 Cassini RADAR altimetric data in Fig. 1. We consider a host-inclusion model made of liquid methane/ethane/nitrogen ($\varepsilon_h' = 1.72$ and $tg\delta = 3.5e^{-5}$) and nitrogen gas bubbles and integrate the SVR model as explained in Section V.A. Horizontal lines refer to particle radii available in the literature. The area highlighted in blue represents the possible radii and densities pair for our case of no volume scattering detection. The lower black solid lines represent the measured SVR and provides the maximum $N_{V,max}$ at a certain particle size, or equivalently, the maximum r at a varying density. The gray dashed lines refer to the uncertainty on the SVR_{meas}, as described in Section V.A and shown in Fig.2 f a) is obtained considering a Gaussian distribution of particles size with std $1e^{-6}$. b) is obtained considering a uniform distribution of particle size and uses a logarithmic scale for both the x and y axis.

TABLE I
NITROGEN GAS – RESULTS SUMMARY

Radius, mm	Reference	Rationale	ND constraint (SVR = 45.92 dB)		Extinction	
			N_V, n/m^3	v_i, %	N_V, n/m^3	v_i, %
0.65	Farnsworth et al. [36]	Experimental Measurement	1.69e^6	0.19	1.4e^7	1.600
0.1	Cordier and Liger-Belair [40]	Lower radius bound	> 8.7e^7	> 10	> 8.7e^7	> 10
2	Hofgartner et al. [19]	BRSA < 1	2500	0.00840	2.0e^4	0.06700
2.5	Cordier and Liger-Belair [40]	BRSA < 1	600	0.00390	5400	0.03500
10	Cordier and Liger-Belair [40]	BRSA < 10 with 100 n/m^3	0.1500	0.00006	1.3000	0.00054
20	Hofgartner et al. [19]	Upper radius bound	0.0025	0.00008	0.0200	0.00067
23	Cordier and Liger-Belair [40]	Breakdown radius	0.0010	0.00005	0.0090	0.00046

by selecting observations featuring seabed detection as shown in Fig.1, where the signal penetrated the whole liquid depth.

V. VOLUME SCATTERING ANALYSIS OF CASSINI ALTIMETRIC DATA

A. SVR measurement

We conduct the SVR measurement on data acquired by Cassini RADAR during T91 flyby over Ligeia Mare, showing a detection of the sea floor at relatively constant depth, as shown in Fig. 2. To take advantage of a wider integration window, we select the bursts where the floor reflection appears to be close to the deepest point ($\sim 160\,m$), accounting for five acquisitions. Notably, the data have been weighted by a Blackman window for sidelobe reduction and seabed detection, both crucial for measuring the volume scattering and to constrain the analysis. This led to a worsening in resolution and resulted in a smaller volume integration window. To compensate for the reduced window size, we applied super-resolution.

Our method involves assessing the presence of a volume scattering signature in the data by comparing the measured SVR and an integrated Signal-to-Noise Ratio, SNR_{int}.
Referring to continuous functions, the volume power within the time window centered at t^* with duration Δt can be expressed as integral of the volume power density, as follows

$$P_V(t^*, \Delta t) = \int_{t^* - \frac{\Delta t}{2}}^{t^* + \frac{\Delta t}{2}} S_V(t)\, dt \quad (21)$$

where the time profile can be equivalently expressed in terms of depth, z.

Due to sampling, the continuous signal assumes the form of a time series, and the measure of volume power can be expressed as

$$P_V = \sum_{i=1}^{m} S_V(i) \quad (22)$$

with $i = 1 \ldots m$ representing the local indexing in the measuring window and m the number of samples within the window.

In this study, P_V is obtained by integration of the normalized altimetric waveforms respect to the surface echo, in an interval Δt = 0.5 μs between 17.0 μs and 17.5 μs to avoid surface and subsurface contributions. The related SVR can be accordingly expressed as the ratio between P_s and P_V as shown in eq. (19).

Being P_V an integral quantity, it is necessary to derive an integral measure of P_N to enable their comparison. We define the integrated noise power $P_{N,int}$ according to eq.(21)

$$P_{N,int}(t^*, \Delta t) = \int_{t^* - \Delta t/2}^{t^* + \Delta t/2} P_N(t) \quad (23)$$

which in the form of a time series assumes the form

$$P_{N,int} = \sum_{i=1}^{m} P_N(i) \quad (24)$$

In order to avoid fluctuations, we compute an averaged version of the noise power $\langle P_{N,int} \rangle$ obtained by averaging the measures from a sliding window

$$\langle P_{N,int} \rangle = \frac{1}{n} \sum_{j=1}^{n} P_{N,int}(j) \quad (25)$$

where *n* is equivalently the number of employed windows and the $P_{N,int}$ measures, and *j* is the lag parameter. The Integrated Signal-to-Noise Ratio SNR_{int} is computed accordingly

$$SNR_{int} = \frac{P_s}{\langle P_{N,int} \rangle} \quad (26)$$

Here, the selected sliding window moves from 12.0 μs to 15.5 μs and has the same size of the integration window used for computing P_V.

After computation and average of P_V and $\langle P_{N,int} \rangle$ values for each of the selected observations in Fig. 2, we obtain a $\langle P_V \rangle$ = $2.55e^{-5}$W and $\langle \langle P_{N,int} \rangle \rangle$ = $2.53e^{-5}$W with an averaged standard deviation (std) of $0.94e^{-5}$W. When comparing with the surface echo, we finally derive an average $\langle SVR \rangle$ = 45.96 dB and a $\langle SNR_{int} \rangle$ = 45.92 dB (refer respectively to the green and gray lines in Fig. 2f). The figure shows that the SVR metric obtained for each observation falls within the 2-σ range of the SNR_{int}, calculated by means of the 2-σ uncertainty on $\langle P_{N,int} \rangle$, and resulting in an asymmetric interval spanning from 43.51 to 51.80 dB, which indicates a lack of significant evidence for volume scattering. Consequently, we infer a maximum value for P_V, or equivalently a minimum value for the SVR equal to SNR_{int}. This enables to individuate a space of possible solutions, as depicted in Fig. 5 and 6, where the SVR_{meas} curve represents an upper limit for both the particle radius and density. More explicitly, such curve describes the maximum size at fixed density and vice versa, according to our model.

Similar considerations can also be extended to data acquired during T108, T104 and T126 flybys over Punga Mare, Kraken Mare and Winnipeg Lacus, where no volume scattering was detected, even with different SNR and SVR measurements.

B. Results and Discussion

With reference to previous studies, we consider a host with a liquid composition of N_2:CH_4:C_2H_6 (with permittivity $\varepsilon'_h = \varepsilon'_{CH4} = 1.72$ and loss tangent $tg\delta = \varepsilon''_h/\varepsilon'_h = 3.5e^{-5}$) coexisting with inclusions of different natures, suspended particles or dissolved gas, that are deemed to be the most plausible in Titan's seas and lakes [13], [29], [57]. We explore the following possible inclusion case-studies:

1. Nitrogen gas (N_2) that, due to the lack of available measurements for its dielectric properties, we model as vacuum bubbles with $\varepsilon'_h = 1$ and $tg\delta = 0$ [40].

2a. Pure solid water ice with $\varepsilon'_h = 3.1$ and $tg\delta = 1e^{-4}$, insoluble in liquid hydrocarbons [58].

2b. Nitriles (acetonitrile, acrylonitrile, cyanoacetylene) which are hypothesized to be at the basin of empty lakes in the form of evaporites [23]. We consider an average $\varepsilon'_h = 2.9$ and $tg\delta = 1e^{-3}$ [29].

2c. Organic aerosol particles, which we assume to have the same properties as Titan-like tholins, an Earth laboratory analogue of Titan organic aerosols [24]. We consider the averages $\varepsilon'_h = 2.2$ and $tg\delta = 1e^{-3}$ [57], [29].

Specifically, using the real part of the dielectric constant and the loss tangent, we calculate the imaginary part of the permittivity. In particular, the model does not incorporate the loss tangent directly; instead, it exploits the real and imaginary components of the permittivity, varied according to Maxwell-Garnett mixing rule (see eq. (9)).

Scenario 1 – Nitrogen gas

Our results are shown in Fig. 5, where the SVR_{meas}= 45.92 dB represents the boundary between two possible cases. The No

TABLE II
SOLID INCLUSIONS ND LIMIT (SVR = 45.92 DB)

	radius, mm	N_V, n/m^3	v_i, %
Water ice	0.33	1.7e^8	2.45
Nitriles	0.49	2.0e^7	1.00
Aerosols	0.84	4.2e^6	1.04

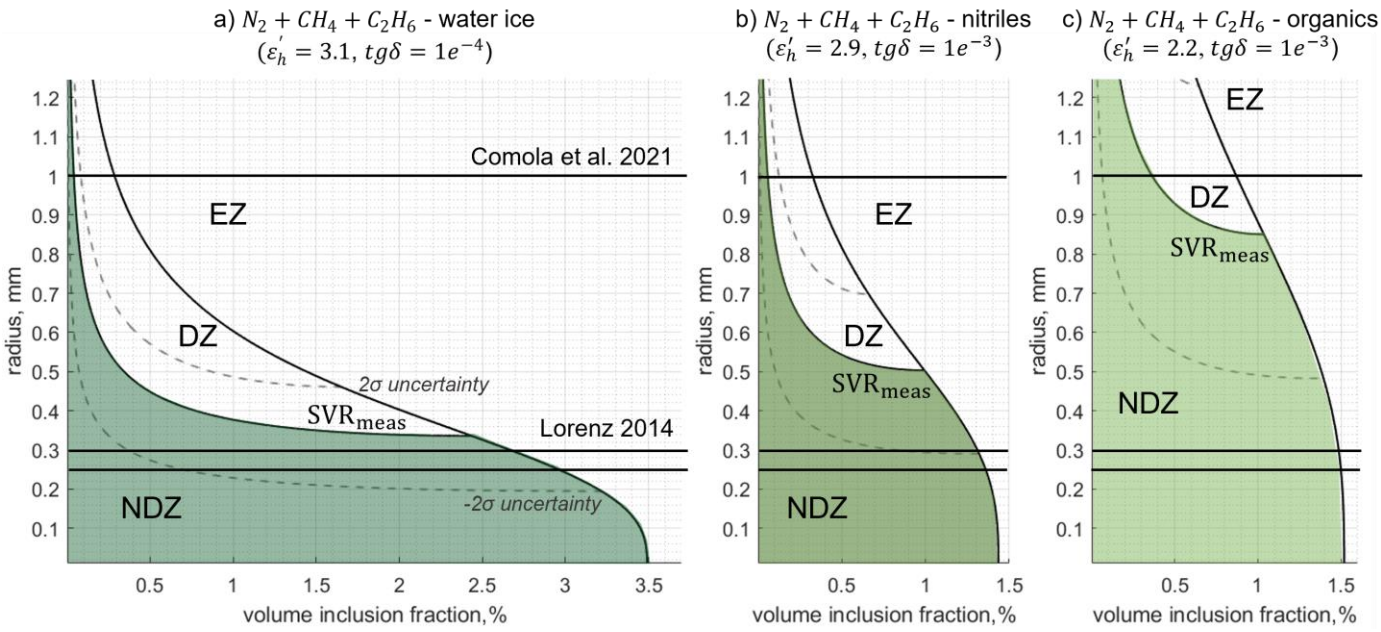

Fig. 6. SVR obtained for three different types of solid spherical inclusions with uniform particle size and where the host is a liquid methane/ethane/nitrogen mixture with permittivity $\varepsilon_h' = 1.72$ and $tg\delta = 3.5e^{-5}$. a) Water ice b) Nitriles c) Organic aerosol particles. Horizontal solid lines refer to particle radii available in literature and estimated considering the techniques listed in Table III.

TABLE III
SOLID INCLUSIONS – RESULTS SUMMARY

Radius, mm	Reference	Scenario	Water ice		Nitriles		Aerosols	
			N_V, n/m³	v_i, %	N_V, n/m³	v_i, %	N_V, n/m³	v_i, %
0.025	Allison 1992 [62]	EZ	5.3e^{11}	3.40	2.2e^{11}	1.43	2.3e^{11}	1.52
0.05	Comola 2021 [70]	EZ	6.6e^{10}	3.49	2.7e^{10}	1.43	2.9e^{10}	1.52
0.05 - 0.15	Lorenz et al. 2006 [5]	EZ	2.4e^{9} - 6.6e^{10}	3.36 - 3.49	1.0e^{9} - 2.7e^{10}	1.42 - 1.43	1.1e^{9} - 2.9e^{10}	1.51 - 1.52
0.09	Greeley & Iversen 1987 [63]	EZ	1.1e^{10}	3.46	4.7e^{9}	1.43	5.0e^{9}	1.52
0.1 – 0.15	Burr et al. 2015a [64] Burr et al. 2015b [65]	EZ	2.4e^{9} - 8.2e^{10}	3.36 - 3.45	1.0e^{9} - 3.4e^{9}	1.42 - 1.43	1.1e^{9} - 3.6e^{9}	1.51 - 1.52
0.125	Lorenz 1995 [66] Kok et al. 2012 [67]	EZ	4.2e^{9}	3.41	1.7e^{9}	1.43	1.8e^{9}	1.51
0.15	Shao and Lu 2000 [68]	EZ	2.4e^{9}	3.36	1.0e^{9}	1.42	1.1e^{9}	1.51
0.25-0.3	Lorenz 2014 [69] Lorenz 2022 [60]	EZ	2.3e^{8} - 4.5 e^{8}	2.66 - 2.96	1.2e^{8} - 2.1e^{8}	1.31 - 1.36	1.3e^{8} - 2.3e^{8}	1.48 - 1.5
1	Comola 2021 [70]	DZ	9.5e^{4}	0.04	1.4e^{5}	0.06	8.3e^{5}	0.35
		EZ	6.9e^{5}	0.29	7.9e^{5}	0.33	2.1e^{6}	0.87
1.25	Sodelbrom 2007 [61]	DZ	2.4e^{4}	0.02	3.7e^{4}	0.03	1.9e^{5}	0.16
		EZ	1.8e^{5}	0.15	2.3e^{5}	0.19	7.7e^{5}	0.63

Detection Zone (ND) encompasses all particles radii and densities combinations when no volume scattering is detected, therefore describing the selected altimetric observations. Alternatively, the Detection Zone (DZ) highlights all possible combinations in the case of detection. The graph also indicates the presence of an Extinction Zone (EZ) (described in Section IV.D). The gray dashed lines, instead, refer to the uncertainty on the SVR_{meas}, as described in Section V.A and shown in Fig.2 f. We incorporate into our graph the results related to particles size obtained from previous theoretical and experimental investigations of nitrogen exsolution phenomena.

Experimental studies of bubbles exsolution under Titan's conditions from Farnsworth et al. provide for a bubble average population of 10 bubbles/cm^2 whose size can be described by a Gaussian distribution with average radius of 0.65 mm and 0.1 mm standard deviation [36]. Such results are obtained at Titan's surface pressure of 1.5 bar, using a liquid depth < 3 cm, therefore they represent a minimum value for bubble size, which could grow under the action of diffusion or coalescence phenomena [40]. Considering a uniform spatial distribution of particles this leads to a volume inclusion fraction of 0.13%. The $\mathrm{SVR}_{\mathrm{meas}}$ at 0.65 mm, according to our model, corresponds to a maximum particle density of approximately 1.691×10^6 bubbles/m^3 (see Fig. 5a), that equates a volume inclusion fraction around 0.19%. We find that, at a bubble radius of 0.65 mm, Cassini RADAR would detect bubbles with a density between 0.17–1.3x10^7 n/m^3. If the bubbles were much more dense, for example 3x10^7 n/m^3, then a bubble with as small as a radius of ~3.5mm would be detected. The larger the bubbles become, the less dense they must be for detection. This suggests that the Cassini RADAR could have observed bubble events only if characterized by marginally bigger size and/or higher density than observed in Farnsworth et al., 2019, up to the signal extinction.

To evaluate the impact of the uncertainty in the host liquid's loss tangent on the maximum density, for the mentioned case, we consider the upper and lower bounds determined by Mastrogiuseppe et al. 2016 and Le Gall which estimate the loss tangent to range between $4.6e^{-5}$ and $2.1e^{-5}$ respectively. This range results in an estimated density variation 1.689×10^6 to 1.694×10^6 bubbles/m^3.

Other theoretical studies model the RADAR backscattering with the aim of understanding radius and concentration to generate the "*Magic Island"* [19], [40]. These studies explore a range of bubble sizes, spanning from fractions of millimeters to few centimeters. They conclude that scenarios with bubble sizes from 0.1 up to 2 - 2.5 mm are unlikely to result in the detection of surficial bright features. These results were reported independently by Hofgartner et al., who analyzed 10000 bubbles within the line of sight, and by Cordier and Liger-Belair, who considered a density of 100 bubbles/m^3. Likewise, our model suggests that bubbles with radius of 0.1 mm would lead to a scenario with no detection and would not incur an extinction within the validity interval of the mixture model. From literature, it is expected that bubble volume inclusion fraction is much lower than 10% [36], [40]. Therefore, under such assumption, Cassini would not be able to detect particles of such size. As shown in Fig. 5b, at the upper radii of 2 and 2.5 mm, our model yields maximum densities of approximately 2500 and 600 bubbles/m^3 to have no detection and 2×10^4 and 5400 bubbles/m^3 for scenarios leading to signal extinction.

According to the same studies, bubbles of larger size and same densities mentioned above would lead to an increase in SAR radar backscattering [40], respectively. These studies consider a maximum bubble radius of 2 cm and 2.3 cm, respectively. For these radii, our model indicates a maximum density of around 0.0025 and 0.001 bubbles/m^3 for no detection and 0.02 and 0.009 bubbles/m^3 for signal extinction. Specifically, Cordier and Liger-Belair estimates that 100 n/m^3 of centimeter sized bubbles would generate the same Bubble Radar Signal Amplification (BRSA) of the "*Magic Island*". According to our model, this scenario would generate no detection with bubble density < 0.15 bubbles/m^3 and lead to extinction with 1.3 bubbles/m^3. A summary of the results is listed in Table I.

The high bubble densities computed from the T92 and T104 SAR data (by [36] and [40] according to the measured BRSA), when compared with the low v_i obtained under standard conditions from T91 altimetric data, strengthen the hypothesis of the Magic Island being generated by ephemeral phenomena.

Scenario 2 – Suspended solids

The solid particles generated in Titan's upper atmosphere ranges in size from fractions to hundreds of microns [59]. Such particles can conglomerate to create larger particles that descend and deposit on Titan's surface, forming dunes, or in the case of seas and lakes, generating sediments and evaporites. Their size is investigated in terms of their mobility as a result of the balance between thermodynamic forces acting against gravity and interparticle cohesion [60]. Several sources along with VIMS spectrometer observations constrain the grains size to a range of 0.05 – 2.5 mm in diameter and are listed in Table III [61], [62], [5], [63], [64], [65], [66], [67], [68]. However, existing studies do not definitively associate the derived grain size to a specific material.

Our results are shown in Fig. 6 for cases 2a), 2b) and 2c) at varying size and inclusion fraction. We find that the detection of suspended particles would be possible if the particles are relatively large (of the order of few millimeters in radius). As expected, at small radii the $\mathrm{SVR}_{\mathrm{meas}}$ and the extinction curves occur at lower inclusion fractions for materials with higher attenuation. Instead, for larger radii, losses are dominated by scattering phenomena, causing an inversion of this behavior. In the three scenarios, particles of size lower than around 0.34 mm, 0.5 mm and 0.84 mm, respectively, are never detected. For densities higher than 2.45%, 1.00% and 1.04% respectively, particles of such sizes lead to extinction without intercepting the $\mathrm{SVR}_{\mathrm{meas}}$ curve for densities higher than 2.45% (1.7×10^8 n/m^3), 1.00% (2×10^7 n/m^3) and 1.04% (4.2×10^7 n/m^3) respectively. Hence, for such cases, our constraint coincides with the extinction scenario as for higher depths the seabed would not be detected. Results are listed in Table II.

With reference to Lorenz 2014 [69], extinction occurs between 2.66% and 2.96% (from 2.3×10^8 to 4.5×10^8 n/m^3), from 1.31% to 1.35% (from 1.2×10^8 to 2.2×10^8 n/m^3), and from 1.48% and 1.5% (from 1.3×10^8 to 2.3×10^8 n/m^3), respectively for the three cases .

With reference to Comola et al. 2021, who suggests a grains of radius 1 mm [70], our model constrain a minimum volume inclusion fraction at 0.04%, 0.06%, and 0.35% (around 9.5×10^4, 1.4×10^5 and 8.3×10^5 n/m^3), for case a), b) and c). Extinction is reached at 0.29%, 0.33%, and 0.87% (6.9×10^5, 7.9×10^5 and 2.1×10^6 n/m^3), respectively. We summarized these results in Table III, along with other estimations at other inclusion sizes available in literature.

VI. Conclusions

In this paper, we conducted a volume scattering analysis of the Cassini RADAR altimetric observations, with the goal of determining the density of potential inclusions in Titan's hydrocarbon lakes and seas. By combining the Mie scattering and radiative equilibrium principles, under the assumption of spherical particles submerged in a liquid, our approach involved the derivation of a mathematical model for describing the Surface-to-Volume power Ratio (SVR) that explicitly incorporate particle size and volume density/inclusion fraction as separate parameters. By keeping one of these parameter constant, we decoupled the other's individual contribution and gained insight of their effect on the SVR.

This inverse modeling technique allowed us to infer particle size and volume density from real Cassini RADAR altimetric observations over Titan's lakes and seas. We selected all the acquisitions featuring seabed detection and measured the SVR within the depths between the two echoes radar returns: from the surface and from the seabed. Upon assessing the absence of volume scattering within the dataset, we infer that the measurement corresponds to the signal SNR, thus indicating a minimum value for the SVR. This enables us to establish a constraint on the maximum inclusion fraction, based on particle sizes derived from previous studies. Four possible host-inclusions mixtures involving (1) nitrogen gas, (2a) water ice, (2b) nitriles and (2c) organic aerosols have been explored.

For nitrogen gas inclusion, laboratory experiments indicated a bubble radius of 0.65 mm, resulting in a maximum volume inclusion percentage of 0.19%. This suggests that detection of such bubbles from the Cassini RADAR would be possible if higher concentration of bubbles or a larger bubbles size is present in Titan's lakes.

Under the hypothesis of solid inclusions, we find that particles with radii lower than around 0.34 mm (for water ice), 0.5 mm (for nitriles) and 0.84 mm (for tholins), respectively with a maximum density of 2.45%, 1.00% and 1.04% cannot be detected without incurring in signal extinction. On the other hand, considering radii in the range 0.025 – 1.25 mm, as Sodelbrom et al. 2007 constrained from VIMS spectrometer observations, we derived a maximum volume inclusion fraction for detection to be between 0.02-3.49%, 0.03-1.43% and 0.16-1.52% for the three materials respectively [61].

Our model can be applied to radar systems onboard present and future missions targeting Jovian and Saturnian moons, such as Europa and Titan, where liquid filled basins are hypothesized to be present [71], [72], [73], [74]. This offers the opportunity to further investigate the properties of such host-inclusion mixtures and gain a deeper understanding of the ongoing processes and composition on these celestial bodies.

Acknowledgments

This research has been developed in the context of the Cassini-Huygens mission, a cooperative endeavor of NASA, ESA, and ASI managed by JPL/Caltech.

Funding support for L.G. was provided by a Doctor of Philosophy Scholarship awarded by Sapienza, University of Rome, and carried out at the Department of Information, Electronic and Telecommunication Engineering (DIET).

The authors want to thank ASI for the past support to the Cassini-Huygens mission and for providing the CPAD SW Tool developed by CORISTA to process the Cassini radar data in altimeter mode.

K.K.F. was predominately supported by an appointment to the NASA Postdoctoral Program at NASA Goddard Space Flight Center, administered by Oak Ridge Associated Universities, under contract with NASA. Additional support was facilitated by the Center for Research and Exploration in Space Science and Technology II (CRESST II) cooperative agreement with NASA and University of Maryland Baltimore County (UMBC), under award number 80GSFC21M0002.

References

[1] C. Elachi, "RADAR: The Cassini Titan radar mapper," Space Science Review, vol. 115, no. 1, pp. 71-110, 2004.

[2] R. M. C. Lopes et al., "Titan as Revealed by the Cassini Radar," *Space Science Reviews* , vol. 215, no. 33, pp. 1-50, 2019, doi: https://doi.org/10.1007/s11214-019-0598-6.

[3] C. Elachi, "Cassini radar views the surface of Titan," Science, vol. 308, no. 5724, pp. 970-974, 2005, doi: 10.1126/science.1109919.

[4] R. D. West e. al., "Cassini RADAR Sequence Planning and Instrument Performance," IEEE Transactions on Geoscience and Remote Sensing, vol. 47, no. 6, pp. 1777-1795, June 2009, doi: 10.1109/TGRS.2008.2007217.

[5] R. D. Lorenz e. al., "The Sand Seas of Titan: CassiniRADAR Observations ofLongitudinal Dunes," *Science,* vol. 312, pp. 724-727, 2006, doi: 10.1126/science.1123257.

[6] J. Radebaugh. e. al., "Dunes on Titan observed by Cassini Radar," *Icarus,* vol. 194, n. 2, pp. 690-703, 2008, doi: https://doi.org/10.1016/j.icarus.2007.10.015

[7] J. Radebaugh. et al., "Mountains on Titan observed by Cassini Radar," *Icarus,* vol. 192, n. 1, pp. 77-91, 2007, doi: https://doi.org/10.1016/j.icarus.2007.06.020.

[8] G. Mitri et al. "Mountains on Titan: Modeling and observations," *Journal of Geophysical Research: Planets,* vol. 115, n. E10, 2010, doi: https://doi.org/10.1029/2010JE003592.

[9] E. Stofan et al., "The lakes of Titan," *Nature,* vol. 445, n. 7123, pp. 61-64, 2007, doi: https://doi.org/10.1038/nature05438.

[10] V. Poggiali et al., "Liquid-filled canyons on Titan," *Geophysical Research Letters,* vol. 43, n. 15, pp. 7887-7894, 2016, https://doi.org/10.1002/2016GL069679

[11] R. H. Brown et al., "The identification of liquid ethane in Titan's Ontario Lacus," *Nature,* vol. 454, pp. 607-610, 2008, doi: https://doi.org/10.1038/nature07100.

[12] M. Mastrogiuseppe et al., "The bathymetry of a Titan Sea," Geophysical Research Letters, vol. 41, no. 5, pp. 1432-1437, 2014, doi: https://doi.org/10.1002/2013GL058618.

[13] M. Mastrogiuseppe et al., "Deep and methane-rich lakes on Titan," Nature Astronomy, vol. 3, no. 6, pp. 535-542, 2017, doi: https://doi.org/10.1038/s41550-019-0714-2.

[14] M. Mastrogiuseppe et al., "Radar Sounding Using the Cassini Altimeter: Waveform Modeling and Monte Carlo Approach for Data Inversion of Observations of Titan's Seas," *IEEE Transactions on Geoscience and Remote Sensing*, vol. 54, no. 10, pp. 5646-5656, Oct. 2016, doi: 10.1109/TGRS.2016.2563426.

[15] M. Mastrogiuseppe e. al., "Bathymetry and composition of Titan's Ontario Lacus derived from Monte Carlo-based waveform inversion of Cassini RADAR altimetry data," *Icarus,* vol. 300, pp. 203-209, 2018, doi: https://doi.org/10.1016/j.icarus.2017.09.009.

[16] M. Mastrogiuseppe e. al., "Cassini radar observation of Punga Mare and environs: Bathymetry and composition," *Icarus,* vol. 496, p. 89–95, 2018, doi: https://doi.org/10.1016/j.epsl.2018.05.033.

[17] V. Poggiali et al., "The bathymetry of moray sinus at Titan's Kraken Mare," *Journal of Geophysical Research: Planets,* vol. 125, n. 12, 2020, doi: https://doi.org/10.1029/2020JE006558.

[18] J. D. Hofgartner et al., "Transient features in a Titan Sea," Nature Geoscience, vol. 7, no. 7, pp. 493-496, 2014, doi: https://doi.org/10.1038/ngeo2190.

[19] J. D. Hofgartner e. al., "Titan's "Magic Island": transient features in a hydrocarbon sea," Icarus, vol. 271, pp. 338-349, 2016, doi: https://doi.org/10.1016/j.icarus.2016.02.022.

[20] A. G. Hayes, R. D. Lorenz and J. I. Lunine, "A post-Cassini view of Titan's methane-based hydrologic cycle. Nature Geoscience, 11(5), 306-313.," *Nature Geoscience*, vol. 11, no. 5, pp. 306-313, 2018, doi: https://doi.org/10.1038/s41561-018-0103-y.

[21] O. Aharonson et al., "Titan's surface geology," in *Titan: Surface, Atmosphere and Magnetosphere*, Cambridge University Press, 2014, pp. 43-75.

[22] J. Barnes e. al., "Organic sedimentary deposits in Titan's dry lakebeds: Probable evaporite," *Icarus,* vol. 216, pp. 136-140, 2011, doi: https://doi.org/10.1016/j.icarus.2011.08.022.

[23] D. Cordier, J. W. Barnes and A. G. Ferreira, "On the chemical composition of Titan's dry lakebed evaporites," *Icarus,* vol. 226, pp. 1431-1437, 2013, doi: https://doi.org/10.1016/j.icarus.2013.07.026.

[24] M. Cable et al., "Titan Tholins: Simulating Titan Organic Chemistry in the Cassini-Huygens Era," *Chem. Rev.* , vol. 112, n. 3, p. 1882–1909, 2012, doi: https://doi.org/10.1021/cr200221x

[25] M. G. Tomasko et al., "Rain, winds and haze during the Huygens probe's descent to Titan's surface", *Nature,* vol. 438, pp. 765-778, 2005, doi: https://doi.org/10.1038/nature04126.

[26] E. C. Czaplinski. et al., "Experimental study of ethylene evaporites under Titan conditions," *ACS Earth and Space Chemistry,* vol. 3, n. 10, pp. 2353-2362, 2019, doi: https://doi.org/10.1021/acsearthspacechem.9b00204.

[27] A. Le Gall. e. al., "Cassini SAR, radiometry, scatterometry and altimetry observations of Titan's dune fields," *Icarus,* vol. 213, n. 2, pp. 608-624, 2011, doi: https://doi.org/10.1016/j.icarus.2011.03.026.

[28] M. Mastrogiuseppe e. al., "Titan dune heights retrieval by using Cassini" *Icarus,* vol. 230, p. 191–197, 2014b, doi: https://doi.org/10.1016/j.icarus.2013.09.028.

[29] A. Le Gall et al., "Composition, seasonal change, and bathymetry," *Journal of Geophysical Review: Planets,* vol. 121, pp. 233-251, 2016, doi: https://doi.org/10.1002/2015JE004920.

[30] P. P. Lavvas, A. Coustenis, I. M. Vardavas, ''Coupling photochemistry with haze formation in Titan's atmosphere, Part I: Model description,'' *Planetary and Space Science,* vol. 56, no. 1, pp. 27-66 , 2008, doi: https://doi.org/10.1016/j.pss.2007.05.026.

[31] P. P. Lavvas, A. Coustenis, I. M. Vardavas, ''Coupling photochemistry with haze formation in Titan's atmosphere, Part II: Results and validation with Cassini/Huygens data,'' *Planetary and Space Science,* vol. 56, no. 1, pp. 67-99 , 2008, doi: https://doi.org/10.1016/j.pss.2007.05.027.

[32] D. Cordier et al. "Structure of Titan's evaporites," *Icarus,* vol. 270, pp. 41-46, 2016, doi: https://doi.org/10.1016/j.icarus.2015.12.034.

[33] J. I. Lunine, "Plausible surface models for Titan," in *Proceedings Symposium on Titan,* Toulouse, 1992.

[34] I. Leifer er al., "Sonar gas flux estimation by bubble insonification: application to methane bubble flux from seep area in the outer Laptev Sea," The Cryosphere, vol. 11, no. 3, pp. 1333-1350, 2017, doi: https://doi.org/10.5194/tc-11-1333-2017.

[35] M. J. Malaska e. al., "Laboratory measurements of nitrogen dissolution in Titan lake fluids," *Icarus,* vol. 289, pp. 94-105, 2017, doi: https://doi.org/10.1016/j.icarus.2017.01.033.

[36] K. K. Farnsworth et al., "Nitrogen exsolution and Bubble Formation in Titan's Lakes," Geophysical Research Letters, vol. 46, no. 23, pp. 13658-13667, 2019, doi: https://doi.org/10.1029/2019GL084792.

[37] I.A. Richardson, J. W. Hartwig and J. W. Leachman, "Experimental effervescence and freezing point depression measurements of nitrogen in liquid methane-ethane mixtures," *International Journal of Thermal Science,* vol. 137, pp. 534-538, 2019.

[38] J. K. Steckloff e. al., "Stratification Dynamics of Titan's Lakes via Methane Evaporization," *The Planetary Science Journal,* vol. 26, 2020, doi: 10.3847/PSJ/ab974e.

[39] D. Cordier, "Bubble stream in Titan's seas as a product of liquid N2+ CH4+ C2H6 cryogenic mixture," Nature Astronomy, vol. 1, no. 5, 2017, doi: https://doi.org/10.1038/s41550-017-0102.

[40] D. Cordier and G. Liger-Belair, "Bubbles in Titan's seas: nucleation, growth and RADAR signature," The astrophysical Journal, vol. 859, no. 1, 2018, doi: 10.3847/1538-4357/aabc10.

[41] S. D. Wall et al., Cassini RADAR Users Guide, 2019.

[42] G. Alberti et al., "The processing of altimetric data (PAD) system for Cassini RADAR," *Mem. SA It. Suppl, 11, 68.*, vol. 1, pp. 1-6, 2004.

[43] K. M. Cuomo, "A bandwidth extrapolation technique for improved range resolution of coherent radar data," MIT Lincoln Lab., Project Rep. CJP60, Revision 1, Dec. 1992.

[44] M. C. Raguso et al., "Super Resolution and Interferences Suppression Technique Applied to SHARAD Data," in *2018 5th IEEE International Workshop on Metrology for AeroSpace (MetroAeroSpace)*, Rome, Italy, 2018.

[45] M. C. Raguso e. al., "Range resolution enhancement of SHAllow RADar (SHARAD) data via bandwidth extrapolation technique: Enabling new features detection and improving geophysical investigation," *Icarus,* vol. 115803, 2023, doi: https://doi.org/10.1016/j.icarus.2023.115803.

[46] L. Gambacorta e. al., "UWB processing applied to multifrequency radar sounders: The case of MARSIS and comparison with SHARAD," IEEE Transactions on Geoscience and Remote Sensing, 60, 1-14.,» *IEEE Trans. Geoscie. and Rem. Sens.*, vol. 60, pp. 1-14, 2022, doi: 10.1109/TGRS.2022.3216893

[47] N. Oudart et al., "Range resolution enhancement of WISDOM/ExoMars radar soundings by the Bandwidth Extrapolation technique: Validation and application to field campaign measurements.," *Planetary and Space science,* vol. 197, n. 105173, 2021, doi: https://doi.org/10.1016/j.pss.2021.105173.

[48] S. Eide et al., "Radar Attenuation in the Shallow Martian Subsurface: RIMFAX Time-Frequency Analysis and Constant-Q Characterization Over Jezero Crater Floor," *Geophysical Research Letters,* vol. 50, n. 7, 2023, doi: https://doi.org/10.1029/2022GL101429.

[49] F. T. Ulaby, R. K. Moore and A. Fung., Microwave remote sensing: Active and passive. volume 1 - microwave remote sensing fundamentals and radiometry, 1981.

[50] F. T. Ulaby, R. K. Moore and A. Fung., Microwave remote sensing: Active and passive. volume 2 - Radar remote sensing and surface scattering and emission theory, 1982.

[51] W. M. Irvine, "Shadowing effects in diffuse reflection," *Journal of Geophysical Research,* vol. 71, no. 12, pp. 2961-2937, 1966, doi: https://doi.org/10.1029/JZ071i012p02931.

[52] G. Picardi et al., "The radar system for the exploration of Titan," Il Nuovo Cimento, vol. 15, pp. 1149-1161, 1992, doi: https://doi.org/10.1007/BF02506709.

[53] M. S. Haynes, "Surface and subsurface radar equations for radar sounders," *Annals of Glaciology,* vol. 61, no. 81, pp. 135 - 142, 2020.

[54] H. Zebker et al.,, "Surface of Ligeia Mare, Titan, from Cassini altimeter and radiometer analysis," *Geophysical Research Letters,* vol. 41, no. 2, pp. 308-313, 2014, doi> https://doi.org/10.1002/2013GL058877.

[55] C. Grima et al., "Surface roughness of Titan's hydrocarbon seas," Icarus, vol. 474, pp. 20-24, 2017.
[56] D. Cordier and N. Carrasco, "The floatability of aerosols and wave damping on Titan's seas," *Nature Geoscience,* vol. 12, n. 5, pp. 315-320, 2019, doi> https://doi.org/10.1016/j.epsl.2017.06.007.
[57] P. Paillou et al., "Microwave dielectric constant of Titan-relevant materials," *Geophsical Research Letter,* vol. 35, pp. 1-4, 2008, doi: https://doi.org/10.1029/2008GL035216.
[58] J. D. Hofgartner a. J. Lunine, "Does ice float in Titan's seas?," *Icarus,* vol. 223, pp. 628-631, 2012, doi: https://doi.org/10.1016/j.icarus.2012.11.028.
[59] S. M. Hörst and M. A. Tolbert, "In situ measurements of the size and density of Titan aerosol analog," *The Astrophysical Journal Letters,* vol. 770, n. 1, 2013, doi: 10.1088/2041-8205/770/1/L10.
[60] R. D. Lorenz, "Sand Transport on Titan: A Sticky Problem," *Geophysical Research Letter,* pp. 1-4, 2022, doi: https://doi.org/10.1029/2022GL098375.
[61] L. Sodelbrom et al.," Correlations between Cassini VIMS spectra and RADAR SAR images: Implications for Titan's surface composition and the character of the Huygens Probe Landing Site,", *Icarus, Planetary and Space Science,* vol. 55, p. 2025–2036, 2007, doi: https://doi.org/10.1016/j.pss.2007.04.014.
[62] M. Allison, "A preliminary assessment of the Titan planetary boundary layer," *Sym. on Titan,* vol. 338, pp. 113-118, 1992.
[63] R. Greleey a. J. D. Iversen, "Wind as a geological process: on Earth, Mars, Venus and Titan", CUP Archive, 1997.
[64] D. M. Burr et al., "Higher-than-predicted saltation threshold wind speeds on Titan," *Nature,* vol. 517, pp. 60-63, 2015, doi: https://doi.org/10.1038/nature14088.
[65] D. M. Burr et al., "The Titan Wind Tunnel: A new tool for investigating extraterrestrial aeolian environments," *Icarus,* vol. 18, pp. 205-214, 2015, doi: https://doi.org/10.1016/j.aeolia.2015.07.008.
[66] R. D. Lorenz, "Prediction of aeolian features on planets: Application to Titan paleoclimatology," *Jour. of Geophy. Res.: Planets,* vol. 100, n. E12, pp. 26377-26386, 1995, doi: https://doi.org/10.1016/j.pss.2007.04.014.
[67] J. F. Kok et al., "The physics of wind-blown sand and dust," Reports on progress in Physics, vol. 75, n. 10, p. 106901, 2012, doi: 10.1088/0034-4885/75/10/106901.
[68] Y. Shao and H. Lu, "A simple expression for wind erosion threshold friction velocity," *Journal of Geophys. Res.: Atmospheres,* vol. 105, n. D17, pp. 22437-22443, 2000, doi: https://doi.org/10.1029/2000JD900304.
[69] R. D. Lorenz, "Physics of saltation and sand transport on Titan: A brief review," *Icarus,* vol. 2013, pp. 162-167, 2014, doi: https://doi.org/10.1016/j.icarus.2013.06.023.
[70] F. Comola et al., "Intermittent saltation drives Mars-like sand transport on Titan," 2021, doi: https://doi.org/10.21203/rs.3.rs-374505/v1.
[71] C. A. Nixon et al., "The Science Case for a Titan Flagship-class Orbiter with Probes,"AGU Fall Meeting, 2020.
[72] G. Mitri et al., "Exploration of Enceladus and Titan: investigating ocean worlds' evolution and habitability in the Saturn system," Experimental astronomy, pp. 1-34, 2021.
[73] S. Rodriguez et al., "Science goals and new mission concepts for future exploration of Titan's atmosphere, geology and habitability: titan POlar scout/orbitEr and in situ lake lander and DrONe explorer (POSEIDON)," *Experimental Astronomy,* vol. 54, n. 2-3, pp. 911-973, 2022.
[74] M. Mastrogiuseppe, "Dual frequency orbiter-radar system for the observation of seas and tides on titan: Extraterrestrial oceanography from satellite.," *Remote Sensing,* vol. 11, n. 16, 2019.

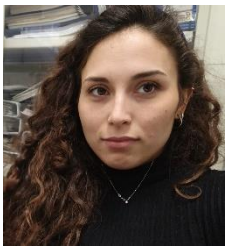

L. Gambacorta received the Bachelor's degree in Aerospace Engineering and the Master's degree in Space and Astronautical Engineering at the *Università degli Studi La Sapienza* of Rome in 2017 and 2020 respectively. She defended her Ph.D. degree in Radar and Remote Sensing at the Department of Information, Electronic and Telecommunications (DIET) in the same university in 2024. Her research interests include the analysis of planetary radar sounder data (MARSIS and SHARAD) for information extraction purposes and the study of data processing techniques oriented to improve sounding capabilities and enhance the quality of the sounder data products.

M. Mastrogiuseppe received the B.S., M. S. and Ph.D. degrees in telecommunication engineering from the University of Rome, Sapienza, in 2005, 2008 and 2012 respectively. From 2014 to 2016, he was Research Associate with the Cornell Center for Astrophysical Science, Cornell University, Ithaca (NY). He is currently researcher with the Dipartimento Elettronica e Telecomunicazioni (DIET), La Sapienza University, Rome. He is the author of several articles. His research interests include remote sensing, radar system, data processing and sounder data analysis for planetary exploration. M. Mastrogiuseppe was nominated as Associate Team Member of Cassini RADAR Science Team. He is team member of SHARAD experiment on board of MRO and Co-Lead of the Visar Instrument onboard of the VERITAS mission for the exploration of Venus.

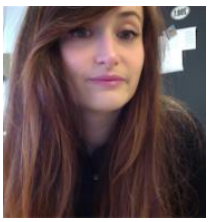

M. C. Raguso received the M.Sc. degree in Communication Engineering and the Ph.D. degree in Radar Systems and Remote Sensing from the University of Rome Sapienza, Rome, Italy, in 2015 and 2018, respectively. From 2015 to 2017, she was Visiting PhD student at the Cornell Center for Astrophysical Science, Cornell University, Ithaca (NY). In 2018, she joined the Geology and Planetary Science Division, California Institute of Technology (Caltech), as a Post-Doctoral Researcher, working on Cassini SAR data. Currently she is a NASA Post-Doctoral Fellow at the Jet Propulsion Laboratory (JPL), California Institute of Technology, Pasadena, CA, USA. Her research interests include radar system data processing, electromagnetic propagation, scattering theory, synthetic aperture radar (SAR), the analysis of planetary radar sounder signals (MARSIS and SHARAD) for geophysical parameter estimation.

V. Poggiali was born in Genoa, Italy, in 1983. He received the M.S. degree in telecommunications engineering in 2011 and the Ph.D. degree (cum laude) in radar and remote sensing from the University of Rome La Sapienza, Rome, Italy, in 2017. He is currently a Senior Research Associate for the Cornell Center for Astrophysics and Planetary Science (CCAPS) in Ithaca, NY, USA. He received the Cassini RADAR Team Group Achievement Award from NASA in 018. His research interests revolve around the use of remote sensing systems for planetary exploration and, in particular, radar systems for the study of Titan, Mars and Earth's Moon.

D. Cordier received the M.Sc. Degree in general physics in 1993 « Agrégation de physique » and served as a physics lecturer in the Ecole le Nationale Supérieure de Chimie de Rennes (ENSCR) between 1994 and 2009. In parallel, he got a PhD degree in stellar physics in 2000 and was a NATO postdoc researcher at the Warsaw Observatory in 2003. Since 2009, he works as a research scientist at the French Center for Scientific Research (CNRS) . His work focuses mainly on surface properties of Titan, he employs numerical models he developed for years.

K. K. Farnsworth was born in Austin, Texas, USA and received a B.S. in Environmental Geosciences with minors in meteorology and geography from Texas A&M University in 2014. In 2020, Dr. Farnsworth earned her Ph.D. in Space and Planetary Science from the University of Arkansas. Following her Ph.D., she became a NASA Postdoctoral Fellow (NPP) at NASA Goddard Space Flight Center (GSFC). Currently, she is continuing her research at NASA GSFC as a Postdoctoral Research Associate at the University of Maryland Baltimore County. Dr. Farnsworth specializes in laboratory simulations of Titan's cryogenic surface, encompassing topics such as, Titan's liquid hydrocarbons, liquid-atmosphere interactions, and hydrolysis reactions in Titan's impact melt pools. Dr. Farnsworth is a Science Team Associate of NASA's New Frontier's mission to Titan, called *Dragonfly*, and is a Collaborator on the OSIRIS-REx Asteroid Sample Return mission.

R.Seu was born in Carbonia (Cagliari), in February 1959. He has got the master's degree in Electronics Engineering in March 1985 at the "'Università degli Studi "La Sapienza" of Rome", and the PhD at the same University in October 1990. Since 1992 and to 2020 he has been assistant professor and presently he is associate professor. He is lecturer of the course of "Radar systems for space applications" and "Systems for air traffic control". Since the doctoral degree he has been always working on radar systems and mainly on radars for planetary observations. Roberto Seu is, since 1993, member of the Cassini Radar Science Team, co-investigator of the experiment.